Fractures and faults across intrusion-induced forced folds: a georesource perspective

Craig Magee
School of Earth and Environment, University of Leeds, UK
0000-0001-9836-2365
Correspondence: c.magee@leeds.ac.uk

Abstract: Intruding magma can create space by uplift and elastic bending of the overburden, which locally fractures the deforming volume and produces flat-topped or dome-like forced folds. Here, I map such fracture networks and quantify their geometry and connectivity across a range of natural and modelled intrusion-induced forced folds. I show that there is a positive relationship between forced fold length and amplitude, and all fracture networks comprise traces, with variable lengths and orientations, that are more intense and denser where fold curvature is greatest. Fracture length populations are typically best described by power-law distributions, but some fit better to log-normal or exponential distributions. Connectivity of fracture networks is low and generally increases with folding, but resurfacing by eruptive products can disrupt this trend. My work supports previous analyses of forced folds and fractures, suggesting that we can use the fracture characteristics of exposed forced folds to predict that of buried forced folds. Due to their geometry and fracture network, intrusion-induced forced folds make ideal fluid traps. As these forced folds are common in many volcanic settings and sedimentary basins, we should consider their potential as exploration targets for water, magmatic-related mineral and metal deposits, and particularly CO_2 storage.

Supplementary material: Text or .svg files containing co-ordinate information of fracture vertices for input into FracPaQ, as well as uninterpreted satellite imagery used, an enlarged version of Figure 5 and all fracture trace and segment length plots are available at https://doi.org/10.6084/m9.figshare.c.6946809

Space for the emplacement of tabular magma bodies (sills and laccoliths), particularly at shallow-levels, is commonly created by uplift of the overlying rock and free surface (e.g. Pollard and Johnson 1973; Segall 2013). This uplift bends the overburden to produce flat-topped or dome-like forced folds, depending on underlying intrusion geometry, and locally induces extension and compression along outer- and inner-arcs, respectively, that drive internal deformation (e.g. fracturing; Fig. 1a) (e.g. Pollard and Johnson 1973; Magee *et al.* 2013; Wilson *et al.* 2021); such forced folds are similar to periclinal folds generated above faults, salt bodies or driven by differential compaction (e.g. Stearns 1978; Cosgrove and Hillier 1999; Lisle 1999; Meng and Hodgetts 2020). Geometrically, forced folds represent four-way dip closures in the subsurface and, like those generated by other mechanisms, those generated above igneous intrusions have been successfully targeted for petroleum exploration and extraction (e.g. Schutter 2003; Rodriguez Monreal *et al.* 2009; Jackson *et al.* 2020). As intrusion-induced forced folds can thus trap fluids, it is worth considering their suitability as potential targets for water, geothermal or mineral/metal exploration, as well as CO_2 storage (e.g. Weis 2012; Scott *et al.* 2015; Montanari *et al.* 2017; Wilson *et al.* 2021).

Drivers of forced folding have limited lateral extents and underlie the deforming rock volume, meaning elastic bending dictates fold development as opposed to buckling, which involves (sub-)horizontal compression (e.g. Pollard and Johnson 1973; Cosgrove and Ameen 1999; Goulty and Schofield 2008). Typically this bending occurs radially about a central point or axis, producing a fold that has a non-zero Gaussian curvature; that is, it is a non-developable surface, like a periclinal fold or dome (Fig. 1a, b) (e.g. Lisle 1999; Mynatt *et al.* 2007). In contrast, most buckle folds form developable surfaces so their Gaussian curvature is zero (Fig. 1b) (e.g. Lisle 1999; Mynatt *et al.* 2007). Some intrusion-induced forced folds, particularly those formed above sub-horizontal sills, have flat tops and monoclinal rims (e.g. Wilson *et al.* 2016), where the Gaussian curvature is non-zero. Having a non-zero Gaussian curvature means forced fold growth induces radial and circumferential tension along outer-arcs, locally instigating internal fracturing and normal faulting of the bending rock volume

From: Kilhams, B., Holford, S., Gardiner, D., Gozzard, S., Layfield, L., McLean, C., Thackrey, S. and Watson, D. (eds)
The Impacts of Igneous Systems on Sedimentary Basins and their Energy Resources.
Geological Society, London, Special Publications, **547**,
https://doi.org/10.1144/SP547-2023-47

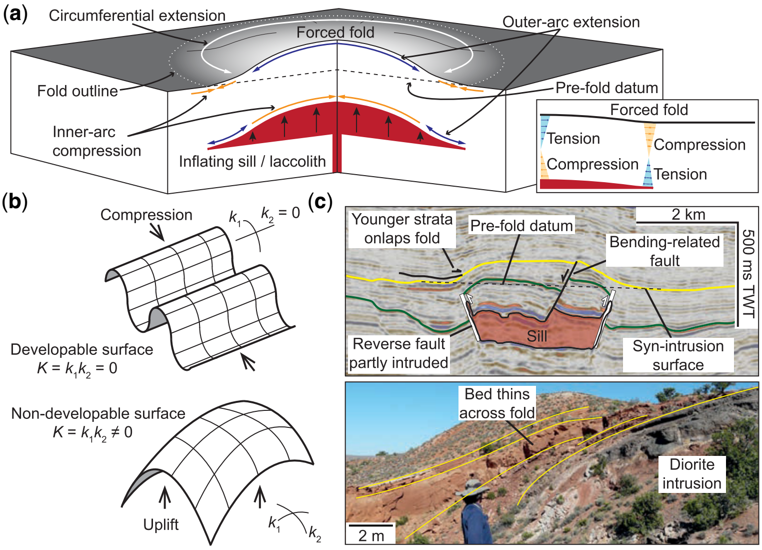

Fig. 1. (**a**) Schematic of a forced fold developed above an inflating sill or laccolith, highlighting areas where outer-arc and circumferential extension occur, and inner-arc compression. The pre-fold datum marks the original surface prior to folding. (**b**) Cartoons showing how buckling creates folds that can typically be described as a developable surface, whereby one of the principal curvatures (k_1, k_2) is zero, meaning the Gaussian curvature (K) is also zero. In contrast, uplift driven by forced folding creates a non-developable surface with non-zero Gaussian curvature (modified from Lisle 1999). (**c**) Seismic reflection image from the Glencoe 3D survey offshore NW Australia depicting a forced fold above a thick sill (same sill as studied by Dobb *et al.* 2022). Field photograph showing forced folding above the dioritic Trachyte Mesa intrusion in the Henry Mountains, Utah. The sandstone beds thin across the fold due to bending-related porosity reduction. Source: (b) modified from Lisle 1999, (c) photograph by Morgan *et al.* 2008.

(Fig. 1a, c) (e.g. Stearns 1978; Cosgrove and Ameen 1999). These tensional stresses become compressional in inner-arc sections, where deformation bands and compaction may occur (Fig. 1a, c) (e.g. Ramsey 1968; Pollard and Johnson 1973; Wilson *et al.* 2021). Critically, the development of tensional and compressional structures within a rock volume can markedly change its porosity and permeability, modifying how it deforms and influencing fluid flow (e.g. Fossen and Bale 2007; Sanderson and Nixon 2015; Dimmen *et al.* 2020). However, few studies have explored how bending-related deformation within intrusion-induced forced folds may affect fluid flow (e.g. Wilson *et al.* 2021).

To assess the suitability of intrusion-induced forced folds as potential exploration or storage targets, for a variety of fluids critical to the energy transition, we need to constrain how their deformation history impacts porosity and permeability (Wilson *et al.* 2021). Here, I build on previous work examining fracture development in forced folds by analysing fracture networks across the top surface of intrusion-induced forced folds (e.g. Cosgrove and Ameen 1999; Pearce *et al.* 2011; Cosgrove 2015; Wilson *et al.* 2021). Specifically, I use satellite imagery and bathymetry data to map faults and fractures across: (1) long-lived forced folds within the Erta'Ale Volcanic Segment, in the Danakil Depression sedimentary basin, Ethiopia (Magee *et al.* 2017); and (2) at Cordón Caulle (Chile) and West Mata (Lau Basin, SW Pacific), where recent individual intrusion events produced new forced folds (e.g. Castro *et al.* 2016; Chadwick *et al.* 2019). I compare these mapped fold and fracture geometries to forced folds recognized in seismic reflection data (Hansen and Cartwright 2006) and generated in physical experiments (Montanari *et al.* 2017, 2020; Henriquet *et al.* 2019; Poppe *et al.* 2019; Warsitzka *et al.* 2022). With these data, I aim to: (1) constrain the fracture network geometrical characteristics of intrusion-induced forced folds; and (2) discuss how understanding and exploring intrusion-induced forced folds, particularly for CO_2 storage, can contribute to the energy transition. Although further research is required to quantify how forced folding affects permeability and porosity, this paper will help inform predictions of subsurface fracture networks within forced folds, and contribute to the assessment of forced folds in georesource exploration and storage.

Case studies

Erta'Ale Volcanic Segment

Situated in the Danakil Depression, a Pleistocene–Recent sedimentary basin comprising a thick sequence of evaporites, the Erta'Ale Volcanic Segment (EAVS) marks one of the final phases of continental breakup along the Red Sea rift (Fig. 2a) (e.g. Bastow *et al.* 2018). The EAVS contains a series of volcanoes surrounded by basaltic to silicic lavas, which primarily emanate from fissures oriented NW–SE (Fig. 2a) (e.g. Watts *et al.* 2020). Spatially associated with several volcanoes in the EAVS are dome-like features, comprising multiple lava flows, that are heavily fractured and faulted: (1) the Alu and Alu South domes are close to and partially underlie the composite Dalafilla stratovolcano, respectively (Fig. 2b) (Pagli *et al.* 2012; Magee *et al.* 2017); (2) adjacent to the Borale'Ale stratovolcano is a sub-circular dome, previously interpreted to be a shield volcano, containing an elliptical central graben that itself hosts a small volcanic vent (Fig. 2c) (Barberi and Varet 1970; Watts *et al.* 2020); and (3) a broad area of uplift beneath the Gada'Ale volcano (referred to as Gada'Ale East) associated with an adjacent, complex dome (referred to as Gada'Ale West), both of which are inferred to be formed due to underlying salt movement (Fig. 2d) (Barberi and Varet 1970). Another dome-like structure,

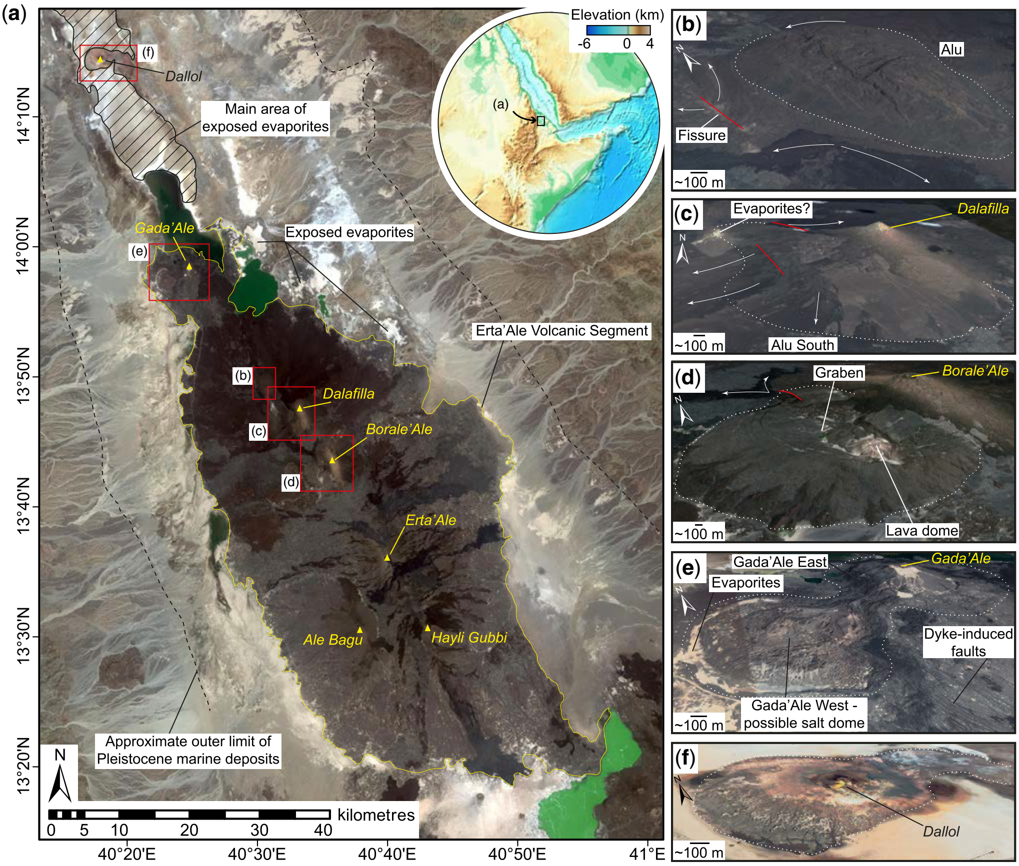

Fig. 2. (**a**) Satellite image of the Erta'Ale Volcanic Segment (EAVS) within the Danakil Depression, Ethiopia, highlighting volcanoes and areas of exposed evaporites. Inset elevation map from the TopoBathy Elevation Tinted Hillshade available through ArcGIS Pro. (**b–f**) Oblique Google Earth views of the (potential) forced folds studied here: Alu, Alu South, Borale'Ale, Gada'Ale East and West and Dallol. Source: (b–f) Image © 2022 CNES/Airbus, Image © 2022 Maxar Technologies; Imagery date: 16 December 2018; Image © 2022 CNES/Airbus, Image © 2022 Maxar Technologies, Image Landsat/Copernicus Imagery date: 17 October 2019; Image Landsat/Copernicus, Image © 2022 Maxar Technologies, Imagery date: 19 February 2011; Image Landsat/Copernicus, Image © 2022 CNES/Airbus, Imagery date: 16 December 2016; and Image Landsat/Copernicus, Image © 2022 CNES/Airbus, Imagery date: 26 February 2019.

comprising evaporite deposits, is present ~30 km north of the EAVS at the Dallol volcano (Fig. 2e) (e.g. López-García *et al.* 2020). Mapping of lava flows that deflect around these domes suggest they formed over the past <80 Kyr (e.g. Fig. 2b) (Magee *et al.* 2017; Watts *et al.* 2020). Ground deformation geodetically detected at these sites, except Borale'Ale, over the past 35 years indicates the domes continue to periodically uplift and subside, likely linked to subsurface magmatism (Amelung *et al.* 2000; Nobile *et al.* 2012; Pagli *et al.* 2012; Albino and Biggs 2021). For example, a 23.2 × 10^6 m^3 lava eruption from a NW-trending fissure ~2 km NW of the Dalafilla stratovolcano summit in 2008 was: (1) preceded by ~9 cm of uplift across Alu over three months; and (2) accompanied by ~1.9 m and ~1 m of subsidence at the Alu and Alu South domes, respectively (Pagli *et al.* 2012). Modelling of this ground deformation suggest Alu and Alu South are underlain by a sill at 1 km depth, possibly with a saucer-shaped geometry, and a larger magma reservoir at 4 km (Pagli *et al.* 2012; Magee *et al.* 2017). Based on their morphology and relation to magmatic or salt movement events, it is plausible that these dome-like features at Alu, Alu South, Borale'Ale, Gada'Ale and Dallol are forced folds (Barberi and Varet 1970; Magee *et al.* 2017).

Cordón Caulle

On 4 June 2011, the rhyolitic volcano Cordón Caulle, Southern Chile, produced an explosive sub-Plinian eruption followed by lava effusion beginning on 15 June (Fig. 3a) (e.g. Castro *et al.* 2016; Wadsworth *et al.* 2022). Between the ~8 June and 3 July 2011, surface elevations in a ~12 km^2 area around the vent site increased by up to ~240 m; these elevation changes can partly be attributed to eruption of a ~35–60 m thick lava, but primarily relate to intrusion-induced surface uplift of previous tephra layers (i.e. forced folding; Fig. 3a) (Castro *et al.* 2016). Modelling this ground deformation suggests uplift was driven by emplacement of a laccolith, with a 0.8–2 km radius and ~0.8 km^3 volume, at a depth of 20–200 m and pressure of 1–10 MPa (Castro *et al.* 2016). Development of the forced fold was accompanied by surface fracturing and faulting (Fig. 3a) (e.g. Castro *et al.* 2016; Wadsworth *et al.* 2022). Subsidence of up to 40 m occurred across the forced fold from August 2011 onwards, and has been related to magma migration out of the laccolith (perhaps coupled with thermal contraction) (Zheng *et al.* 2020) or sintering of pyroclasts during intrusion growth (Wadsworth *et al.* 2022).

West Mata

The West Mata submarine volcano is located between the NE Lau Spreading Centre and the Tofua Volcanic Arc near Fiji and Samoa in the SW Pacific (Fig. 3b) (Chadwick *et al.* 2019). Towards the NE of the volcano base, bathymetric depths decreased by up to 64 m across a 0.73 × 10^6 m^2 area over some period between 2012 and 2016 (Chadwick *et al.* 2019). Part of this depth change can be attributed to emplacement of lava from a NE–SW trending fissure, but most relates to uplift of seafloor sediments and creation of a dome (forced fold) bisected by numerous fractures (Fig. 3b) (Chadwick *et al.* 2019).

'Fold B'

Seismic reflection data reveal 'Fold B' is a dome-shaped forced fold, 3.5 km in diameter and up to ~250 m high, developed ~1 km above a 3 × 2.5 km, up to ~300 m thick, saucer-shaped sill (Hansen and Cartwright 2006, their fig. 4). This sill-fold pair is situated in the NE Rockall Basin and formed in the Late Paleocene-to-Early Eocene within a siliciclastic sedimentary succession (Hansen and Cartwright 2006). A series of normal faults crosscut the forced fold (Hansen and Cartwright 2006, their fig. 10).

Methodology

I use Google Earth and ArcGIS Pro World imagery of different vintages to map linear features across forced folds in the EAVS and at Cordón Caulle, at a resolution of ~30 m (Figs 2, 3a & 4a). For West Mata, I use high-resolution (~1 m) bathymetry data collected using a multibeam sonar system on the autonomous underwater vehicle *Sentry* during part of a two-leg expedition by the *R/V Falkor* crew in 2017 (Fig. 3b) (Chadwick *et al.* 2019). For each forced fold, I manually map the linear features, which are often highlighted by shadows, at a scale of ~1:2000 (e.g. Fig. 4a). In addition to mapping these intrusion-induced forced folds, I analyse a fracture/fault map produced by Hansen and Cartwright (2006) for a forced fold ('Fold B') imaged in 3D seismic reflection data. The seismic reflection survey (T38) used to map this 'Fold B' has a vertical and horizontal resolution of up to ~68 m, if we consider each is equivalent to a quarter of the seismic wavelength ($\lambda/4$) (Hansen and Cartwright 2006; Brown 2011). I also generate fold and fracture maps for physical experiments using select published images (Montanari *et al.* 2017, 2020; Henriquet *et al.* 2019; Poppe *et al.* 2019; Warsitzka *et al.* 2022).

Forced fold measurements

To provide context for fracture network assessment, I first analyse forced fold geometry. Where fold

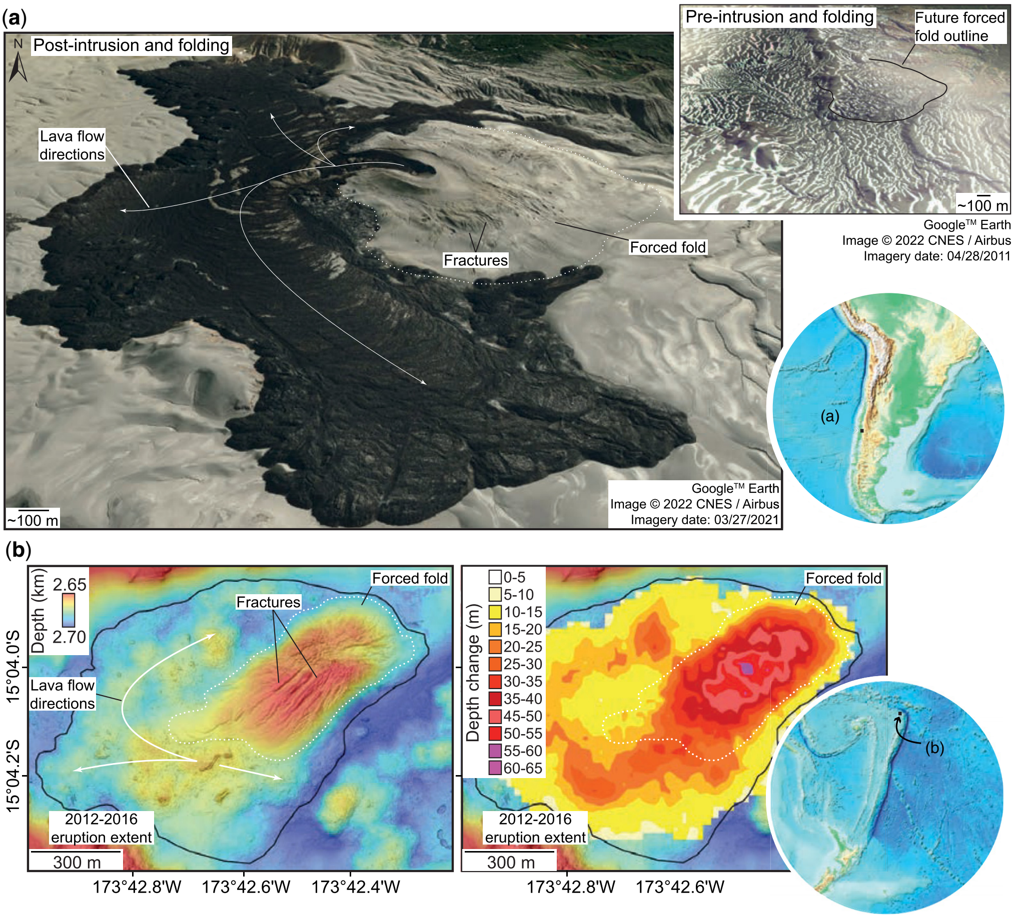

Fig. 3. (**a**) Google Earth imagery of the Cordón Caulle forced fold, from before (April 2011; inset image) and after its development in July 2011. (**b**) Bathymetry map of the forced fold developed at West Mata, and a map showing the change in depth across the fold and surrounding lava flow. Inset elevation maps for (a–b) from the TopoBathy Elevation Tinted Hillshade available through ArcGIS Pro. Source: (a) Google Earth image (2022 CNES/Airbus), (b) modified from Chadwick *et al.* 2019.

outlines can be confidently identified in the remote sensing data and model images, I measure fold length, width and map-view area (A). I also measure fold amplitudes where elevation data, or cross-sections through the folds, are available; for these measurements, I assume that the pre-fold datum follows the regional trend of the current free surface outboard of the fold outline (e.g. Fig. 1a, c). However, there are some uncertainties in the measurement of forced fold length and amplitude: (1) we can rarely establish the original surface topography prior to emplacement and folding, so often cannot accurately constrain true amplitudes; (2) syn- or post-emplacement deposition of sediments or resurfacing by lavas may alter apparent forced fold heights or regional base levels (e.g. Dobb *et al.* 2022; Warsitzka *et al.* 2022); (3) fold crests may have been eroded (e.g. Hansen and Cartwright 2006); and/or (4) measurements from 2D seismic reflection data, which are rarely depth-converted and decompacted (Magee *et al.* 2019), or physical model cross-sections may not intersect forced fold maximum amplitude or length (e.g. Jackson *et al.* 2013).

For the EAVS forced folds, available Shuttle Radar Topography Mission (SRTM) 1 Arc-second global data allow me to measure their current surface area (A_i). Comparing the map-view and current surface area measurements of the EAVS forced folds provides an estimate of the extensional strain across the fold tops. From this SRTM data, I also calculate the Gaussian curvature (K; Fig. 1b) of the EAVS folds by extracting a point cloud grid, with spacings of 30 m, for import into the PyVvista module for

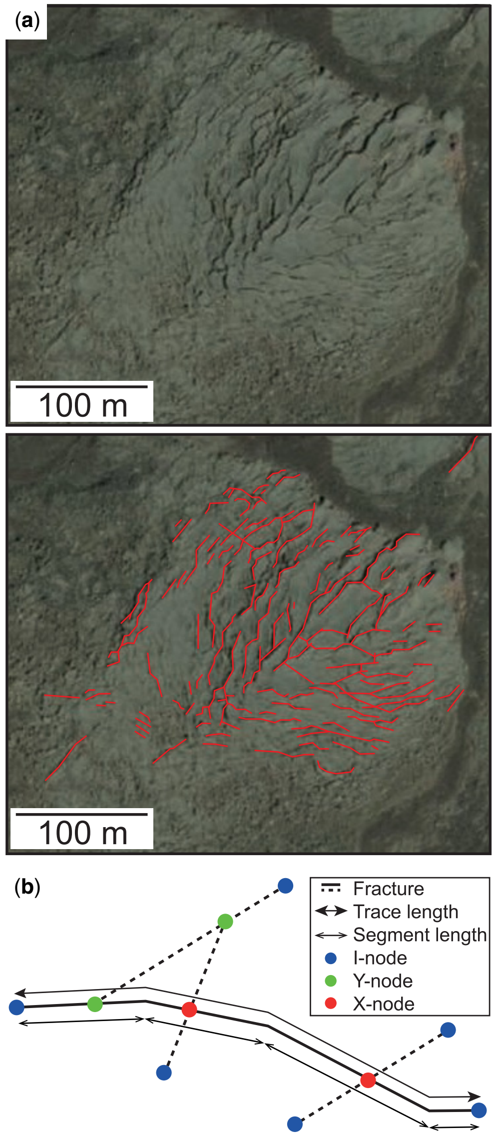

Fig. 4. (**a**) Uninterpreted and interpreted zoomed-in image of an intense zone of fractures, often depicted by shadows, on the Alu South dome (see Fig. 5 for location). (**b**) Schematic showing fracture trace and segment definition, as well as I-, Y-, and X-node characterization. Source: (a) © 2022 CNES/Airbus, Image © 2022 Maxar Technologies, Image Landsat/Copernicus Imagery date: 17 October 2019.

Python (Sullivan and Kaszynski 2019); forced folds elsewhere were not analysed with this method as their respective data were not in suitable formats. PyVista takes the X, Y, Z co-ordinate data of the point cloud to create a mesh (Sullivan and Kaszynski 2019), and then calculates the Gaussian curvature of each node from their principal curvatures (k_1, k_2; Fig. 1b) (Lisle 1999).

Fracture analyses

I interpret the linear features across the studied forced folds as fractures and faults, but acknowledge some may have developed before or after folding or could be related to fluvial incision (e.g. Henriquet *et al.* 2019), gravitational collapse, presence of other structures (e.g. deformations bands) and/or processing artefacts. Although some linear features may thus not relate to extension during folding, I note that: (1) fractures can focus fluvial incision, meaning any channels mapped may be a proxy for fracture locations (Henriquet *et al.* 2019); and (2) gravitational processes could affect the long-term distribution of fractures in folds. Overall, without ground-truthing, my fracture maps cannot be validated.

From the fracture and fault maps I create, I use FracPaQ software to analyse their network properties, such as trace and segment line length and strike, fracture intensity and density, and connectivity (Fig. 4b) (Healy *et al.* 2017). Because the entire traces of all resolved fractures are can be mapped across the forced folds, which have 100% exposure, no adjustments are required to account for fractures extending beyond study limits or those that may occur in areas of limited coverage (cf. Sanderson and Nixon 2015). Deriving fracture trace and segment length distributions is critical to predicting fracture network attributes at smaller or larger scales (e.g. Rizzo *et al.* 2017). These distributions are statistically analysed in FracPaQ using maximum likelihood estimators, which establishes the probability of whether the data is best-fit by power-law, log-normal, or exponential distributions (Healy *et al.* 2017; Rizzo *et al.* 2017).

In addition to examining fracture lengths, I measure fracture intensity (P21), which describes the total fracture length in set area, and fracture density (P20), which measures the number of fractures in the same area (Sanderson and Nixon 2015; Healy *et al.* 2017); these parameters are calculated using a circular scan window method (Healy *et al.* 2017), but only assessed for natural forced folds because the number of fractures created in modelled forced folds is generally too low to be statistically meaningful. As Gaussian curvature is a measure of 3D strain, fracture intensity and density should increase where K is greatest (Lisle 1999).

To assess network connectivity, FracPaQ identifies I-, Y-, and X-nodes of fractures, whereby I-nodes correspond to isolated fracture tips, Y-nodes occur where one fracture abuts another, and X-nodes where fractures crosscut each other (Fig. 4) (Sanderson and Nixon 2015; Healy *et al.* 2017). All node maps obtained from FracPaQ were manually verified and adjusted where needed. From the number of these nodes ($N_{\mathrm{I,Y,X}}$) per forced fold, I calculate the number of lines bound by I- and Y-nodes (N_{L}), the number of branches (N_{B}) defining portions of fractures bound by any two nodes, the average number of connections per line (C_{L}), and the average number of branches per line (C_{B}) (Sanderson and Nixon 2015):

$$N_{\mathrm{L}} = 0.5(N_{\mathrm{I}} + N_{\mathrm{Y}})$$

$$N_{\mathrm{B}} = 0.5(N_{\mathrm{I}} + 3N_{\mathrm{Y}} + 4N_{\mathrm{X}})$$

$$C_{\mathrm{L}} = 2(N_{\mathrm{Y}} + N_{\mathrm{X}})/N_{\mathrm{L}}$$

$$C_{\mathrm{B}} = (3N_{\mathrm{Y}} + 4N_{\mathrm{X}})/N_{\mathrm{B}} \tag{1}$$

Both C_{L} and C_{B} are useful indicators of connectivity (Sanderson and Nixon 2015; Healy *et al.* 2017). For example, simulated percolation of randomly oriented lines of a fixed length occurs at $C_{\mathrm{L}} = 3.57$ (Sanderson and Nixon 2015).

Results

The studied natural forced folds are circular to elliptical, with length to width aspect ratios of ~1.00–2.05, and they have amplitudes, lengths and map areas that range from ~40–368 m, ~0.9–4.1 km, and ~0.27–16.01 km^2, respectively (Figs 2, 3, 5 & 6; Table 1). For those in the EAVS, comparison of map-view area and current surface area measurements suggests the top of the forced folds have increased in size by 0.1–4.97% during uplift (Table 1). There is a weak, positive power-law relationship between fold length and maximum amplitude of the natural forced folds studied ($R^2 = 0.13$), but this fit increases if the Dallol forced fold is excluded ($R^2 = 0.51$) (Fig. 7). Dallol has a length to maximum amplitude ratio of 138, whereas the other natural forced folds studied range from 10 to 21 (Table 1). For forced folds produced in physical models (Fig. 8; Table 2), there also appears to be a moderate, positive power-law relationship between the fold length and amplitude ($R^2 = 0.66$) where these data are available (Fig. 7). The power-law fit between all natural and modelled forced fold lengths and amplitudes, including those reported in previous work, is strong ($R^2 = 0.89$) and positive (Fig. 7).

The fractures and their constituent segments mapped along the top of the natural forced folds vary in number and length (Figs 5, 6 & 9; Table 1; Supplementary Figs S3 and S4). Segment numbers and total trace length are particularly low for the seismically imaged ‘Fold B’ (253 segments totalling 2.376 km long), compared to those observed in satellite or bathymetry data, for which 758–4160 segments are mapped and total trace lengths are ~13.4–114.6 km (Figs 5 & 9; Table 1). Within each natural forced fold, there is typically a relatively reduced amount of fracture traces or segments at small length fractions, particularly for ‘Fold B’ (Fig. 9; Supplementary Figs S3 and S4). The probability that the length distributions of these fracture populations describe log-normal, power-law or exponential relationships is often similar, but: (1) the probability that trace or segment lengths define power-law distributions is always >95%; and (2) for some forced folds, the probability that trace and segment lengths define a log-normal (e.g. Alu South) or exponential (e.g. Gada’Ale West) distribution is relatively low (<80%) (Fig. 9; Table 3; Supplementary Figs S3 and S4). There is a moderate, positive power-law relationship between fold area and total trace length of the natural forced folds excluding ‘Fold B’ ($R^2 = 0.55$), and those physical models where these geometry parameters are reported ($R^2 = 0.60$); the power-law fit between the natural and model forced folds is strong ($R^2 = 0.98$) (Fig. 10; Tables 1 & 2).

The fracture networks, including those observed across modelled forced folds, typically show a broad range of strike orientations, although many contain fracture populations preferentially oriented sub-parallel to the fold long axes (Figs 5, 6 & 8). Fracture distributions are also variable across individual forced folds (Figs 5, 6 & 8); for example, fracture intensity and density typically appear greatest where major normal faults are developed (e.g. in Borale’Ale) and/or Gaussian curvature is highest (Figs 5 & 6). The connectivity of the studied fracture systems in natural forced folds is low ($C_{\mathrm{L}} < 1.31$ and $C_{\mathrm{B}} < 1.17$), being dominated by I-nodes and containing <10% X-nodes (Figs 5, 6 & 11a; Table 2). Connectivity of fracture networks produced within modelled forced folds is also typically low but does increase up to C_{L} values of 3.01 and C_{B} values of 1.66 (Fig. 11a; Table 3). Where physical models provide constraints on how fracture networks developed through time, it is clear that connectivity generally increases via the proportional formation of more Y- and X-nodes following power-law (e.g. SPCTIN06; $R^2 = 0.78$) or exponential (e.g. Exp1B; $R^2 = 0.80$) relationships (Fig. 11). However, decreases in connectivity can occur when eruptions resurface the folds (e.g. Fig. 11b).

Discussion

As the four-way dip closure form of intrusion-induced forced folds can trap fluids (e.g. Schutter 2003; Rodriguez Monreal *et al.* 2009), and these

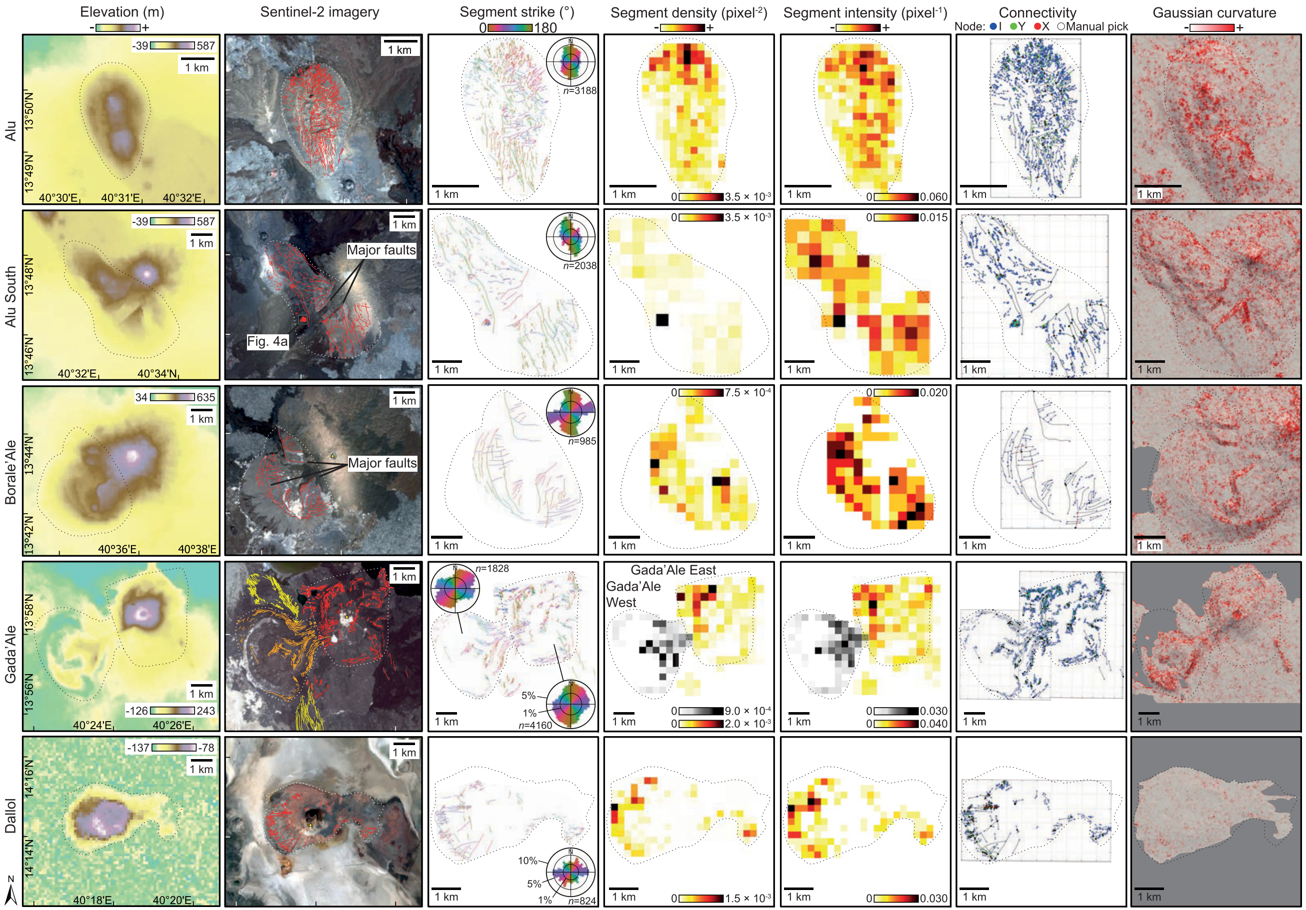

Fig. 5. Compilation of maps for the EAVS forced folds highlighting their elevation (SRTM data) and fracture patterns. Maps of fracture segment strike (with associated rose diagrams where *n* is the number of segments), density, and intensity are also provided, along with fracture connectivity. Gaussian curvature is also shown. See Supplementary Figures S1 and S2 for an enlarged version and uninterpreted remote sensing data, respectively. Source: Copernicus Sentinel-2 imagery data (2015) retrieved from ArcGIS Pro, processed by ESA

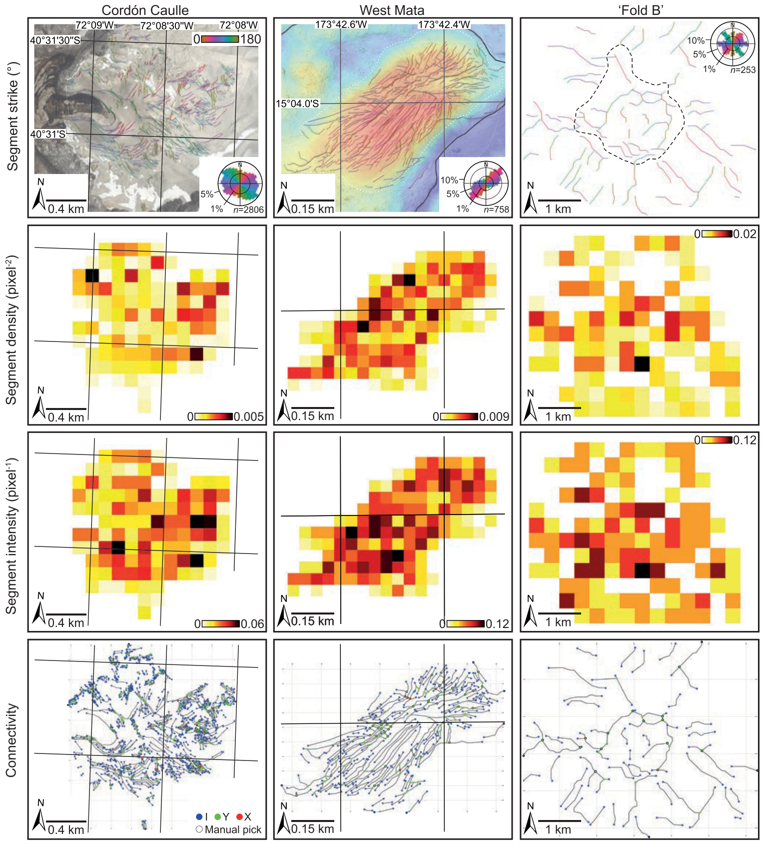

Fig. 6. Compilation of maps for Cordón Caulle, West Mata, and 'Fold B' showing their fracture segment strike (with associated rose diagrams where *n* is the number of segments), density, intensity, and connectivity. See Supplementary Figure S2 for uninterpreted remote sensing data.

structures are present in many sedimentary basins and active volcanic settings worldwide (e.g. Pollard and Johnson 1973; Holford *et al.* 2012; van Wyk de Vries *et al.* 2014; Magee *et al.* 2016, 2017; Tian *et al.* 2021; Kumar *et al.* 2022), we should consider them as potential fluid storage sites. For example, their association with magmatism means intrusion-induced forced folds may trap hydrothermal fluids, creating: (1) suitable geothermal energy exploration targets in active volcanic settings (e.g. Scott *et al.* 2015; Montanari *et al.* 2017); or (2) important mineral/metal accumulations, such as porphyry copper deposits (e.g. Weis 2012). Ancient intrusion-induced forced folds may also host aquifers (e.g. Wilson *et al.* 2021), or could potentially provide suitable CO_2 storage sites (cf. Tueckmantel *et al.* 2012). Critically, forced folding involves bending of a rock volume, which locally induces internal fracturing and faulting, thereby modifying permeability (e.g. Jackson and Pollard 1990; Cosgrove and Ameen 1999; Wilson *et al.* 2021). These changes in permeability can enhance the fluid storage potential of these traps, but can lead to breaching and fluid leakage (see Cosgrove 2015 and references therein). To appraise whether intrusion-induced forced folds may provide suitable fluid storage sites, we need to establish how their evolution affects fracture connectivity, which controls host-rock permeability (e.g. Sanderson and Nixon 2015; Wilson *et al.* 2021). Furthermore, because many intrusion-induced forced fold exploration targets may be subsurface, we may lack the direct information necessary to properly characterize the geometry and growth of their fracture network. Stochastic models are thus required to simulate potential fracture patterns and their impact on fluid flow, which themselves need to be underpinned by statistical characterization of natural fracture networks (e.g. Riley 2005). Here, I discuss how driving mechanisms relate to and control forced fold geometry and fracture networks, and what implications these have for the role forced folds may play in the energy transition.

Table 1. Natural forced fold geometry and fracture networks

Location	Forced fold geometry								Total fracture length (km)	Fracture connectivity							
	Length (km)	Width (km)	Length: width	Map area (km^2)	Surface area (km^2)	Strain (%)	Maximum amplitude (m)	Length: amplitude		I	Y	X	N_L	N_B	N_L/ N_B	C_L	C_B
Alu	3.44	2.05	1.68	05.07	05.32	4.97	341	10	070.43	1755	275	17	1015	1324	1.30	0.58	0.67
Alu South	6.78	3.39	2.00	16.01	16.36	2.22	320	21	062.95	1166	129	16	0648	0809	1.25	0.45	0.56
Borale'Ale	4.99	4.11	1.22	15.27	15.63	2.41	368	14	037.77	0174	008	11	0091	0121	1.33	0.42	0.56
Gada'Ale East	4.27	3.83	1.11	13.50	11.52	1.97	366	12	068.66	2146	371	30	1259	1690	1.34	0.64	0.73
Gada'Ale West	4.46	3.70	1.20	11.30	13.61	0.82	180	25	114.56	0806	191	10	0499	0710	1.42	0.81	0.86
Dallol	5.51	3.29	1.68	11.70	11.71	0.10	040	138	035.49	0384	112	50	0248	0460	1.85	1.31	1.17
Cordón Caulle	2.13	1.80	1.18	02.99	–*	–	200	11	046.23	1313	360	18	0837	1233	1.47	0.90	0.93
West Mata	0.90	0.44	2.05	00.27	–	–	064	14	013.44	0343	134	05	0239	0383	1.60	1.17	1.10
'Fold B'	3.50	3.50	1.00	13.00	–	–	250	14	002.37	0103	022	00	0063	0085	1.35	0.70	0.78

*Indicates measurements could not be acquired from available data.

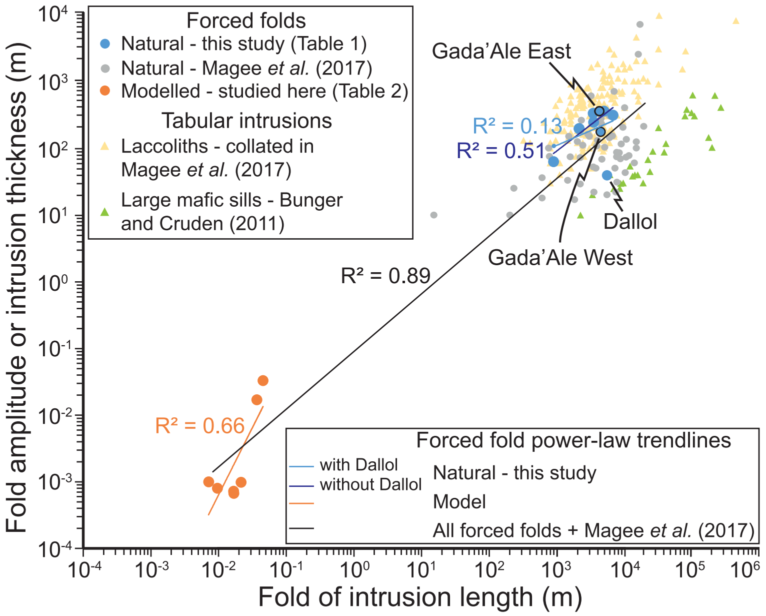

Fig. 7. Plot of fold length and amplitude for the studied forced folds, including those created in physical models (orange circles) where this information is provided or can be extracted (see Tables 1 & 2 for data). Forced fold (grey circles) and tabular intrusion (yellow and green triangles) measurements from other studies are also shown (data collated by and presented in Magee *et al.* 2017).

Intrusion-induced forced folding

Emplacement of tabular sills and laccoliths at shallow levels commonly drives roof uplift, producing forced folds that are often bisected by extensional fracture and normal fault networks (e.g. Pollard and Johnson 1973; Magee *et al.* 2013, 2017; Segall 2013; van Wyk de Vries *et al.* 2014; Wilson *et al.* 2016). Compilations of dimensional data for laccoliths and large mafic sills show they have length to thickness ratios of ~1.7–45 and ~200–2000, respectively, defined by a power-law relationship (Fig. 7) (e.g. McCaffrey and Petford 1997; Bunger and Cruden 2011; Cruden *et al.* 2018). Previous studies of forced folds show their lengths and maximum amplitudes typically overlap with and span the gap between the lower size ranges of laccoliths and large mafic sills (Fig. 7) (see Magee *et al.* 2017 and references therein). Assuming these forced folds are geometrically similar to their underlying intrusion, the distribution of their lengths and amplitudes suggests there is a spectrum in tabular magma body shape between laccolith and large mafic sill end-members (Fig. 7).

Most of the natural forced folds studied here have a length and maximum amplitude relationship defined by a moderate power-law relationship ($R^2 = 0.51$), and ratios (10–21) similar to that of laccoliths (Fig. 7). The forced fold at Dallol has a size and length to maximum amplitude ratio (138) similar to a large mafic sill (Fig. 7). Overall, there is a strong, positive relationship ($R^2 = 0.89$) between length and maximum amplitude of all natural and modelled forced folds (Fig. 7) (see also Magee *et al.* 2017). These observations suggest forced fold geometry, including curvature, is scale invariant (see McCaffrey and Petford 1997; Bunger and Cruden 2011; Cruden *et al.* 2018). Furthermore, the similarity between intrusion-induced forced folds at Alu, Alu South, Cordón Caulle and West Mata (Pagli *et al.* 2012; Castro *et al.* 2016; Magee *et al.* 2017; Chadwick *et al.* 2019), and the Gada'Ale East and West domes (Figs 5, 7, 9 & 11), which have been attributed to underlying salt movement (Barberi and Varet 1970), could be suggest that: (1) the Gada'Ale folds also formed in response to magma (and salt?) movement, consistent with recognition of recent dyke-related uplift near Gada'Ale East (Amelung *et al.* 2000); or (2) the geometry and fracturing of forced folds is not diagnostic of their driving mechanism (i.e. salt- and magma-driven forced folds are similar). It thus seems reasonable to consider exposed or modelled forced folds as suitable analogues of forced folds in the subsurface (e.g. Gholipour *et al.* 2016). Improving confidence in understanding similarities between buried and exposed or modelled forced folds is important because it underpins whether we can use fracture

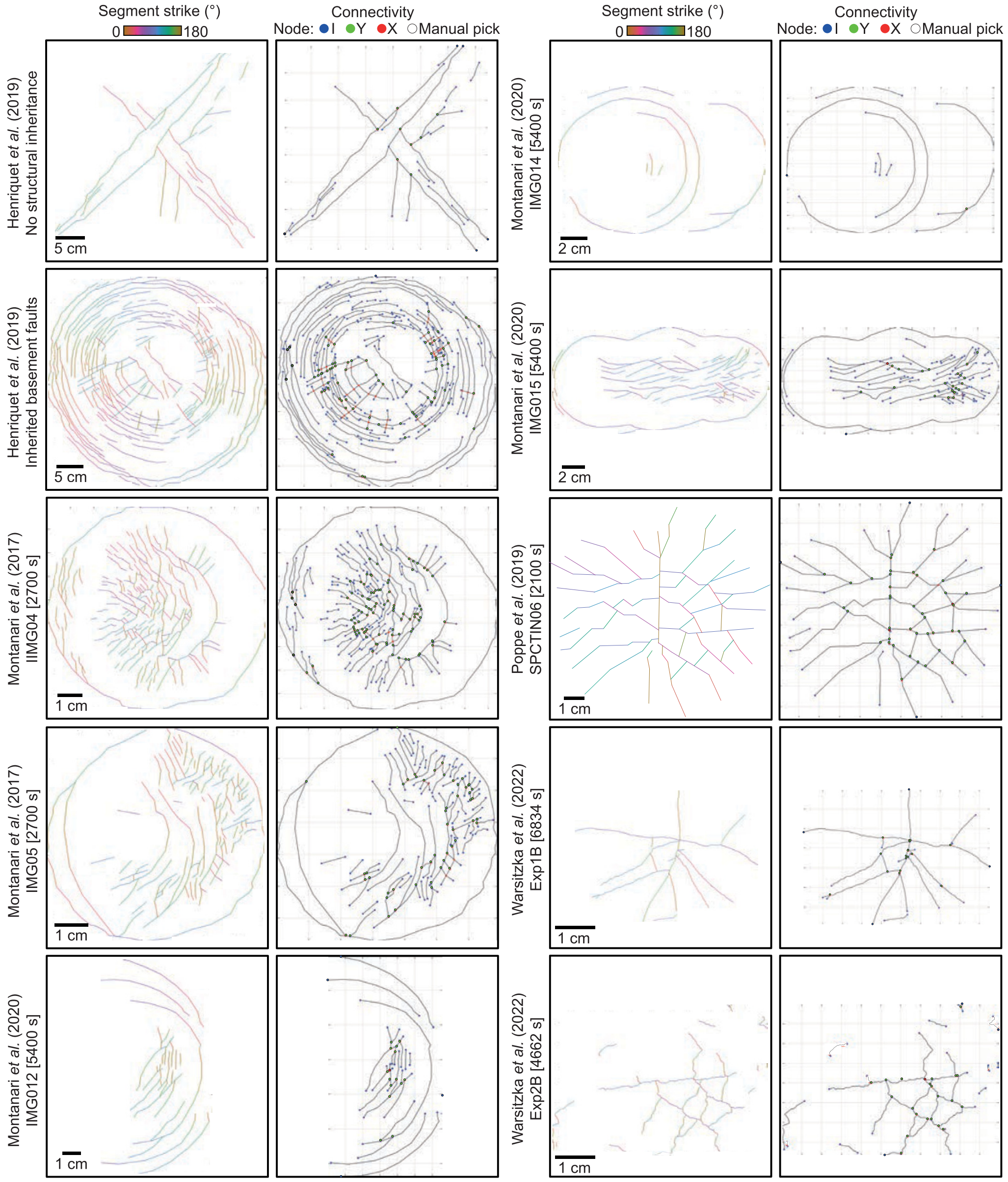

Fig. 8. Segment strikes and fracture connectivity maps of the physical model forced folds studied. All maps show the fracture networks at their most developed. No experiment duration is provided for the Henriquet *et al.* (2019) models, but the timestamp of other models is shown in seconds (s).

network observations to predict their characteristics in the subsurface and/or at different scales.

Intrusion-induced forced fold fracturing

The fracture networks of all the studied forced folds qualitatively appear similar, regardless of the host rock lithology; that is, they all contain fractures and faults of variable orientation and length, which increase in intensity and density with fold curvature (Figs 5, 6 & 8; Table 1). Previous studies examining fracturing across periclinal folds created by forcing mechanisms, other than magma emplacement, also describe similar fracture networks characteristics (e.g. Stearns 1978; Cosgrove and Ameen 1999; Lisle 1999; Cosgrove 2015). My findings thus

Table 2. Modelled forced fold geometry and fracture networks

References	Model	Time (s)	Forced fold geometry						Total fracture length (km)	Fracture connectivity							
			Length (cm)	Width (cm)	Length: width	Area (cm^2)	Maximum amplitude (cm)	Length: amplitude		I	Y	X	N_L	N_B	N_L/ N_B	C_L	C_B
Henriquet *et al.* (2019)	Inherited basement faults	?*	368.48	293.11	1.26	0848.28	17.000	1	02.45	036	07	00	022	029	1.33	0.65	0.74
	No structural inheritance	?	456.84	440.83	1.04	1581.71	33.000	1	10.69	245	75	30	160	295	1.84	1.31	1.17
Montanari *et al.* (2017)	IMG04	?	–[†]	–	–	–	–	–	00.10	010	02	00	006	008	1.33	0.67	0.75
		?	075.53	071.03	1.06	0042.13	–	–	00.49	117	22	00	070	092	1.32	0.63	0.72
		?	074.36	069.15	1.08	0040.39	–	–	00.75	168	43	04	106	157	1.48	0.89	0.93
		?	093.47	079.75	1.17	0058.55	–	–	01.34	147	73	03	110	189	1.72	1.38	1.22
		2700	096.92	088.58	1.09	0067.42	00.800	12	01.38	129	97	05	113	220	1.95	1.81	1.41
	IMG05	?	057.20	050.79	1.13	0022.82	–	–	00.54	110	39	03	075	120	1.60	1.13	1.08
		?	060.02	054.26	1.11	0025.58	–	–	00.85	129	51	08	090	157	1.74	1.31	1.18
		?	069.77	062.01	1.13	0033.98	–	–	01.02	109	52	07	081	147	1.82	1.47	1.26
		2700	071.70	066.70	1.08	0037.56	01.000	7	00.89	106	51	67	079	264	3.36	3.01	1.60
Montanari *et al.* (2020)	IMG12	?	–	–	–	–	–	–	00.10	006	00	00	003	003	1.00	0.00	0.00
		?	–	–	–	–	–	–	00.42	019	02	01	011	015	1.38	0.57	0.69
		5400	168.20	–	–	–	00.719	23	00.73	036	14	01	025	041	1.64	1.20	1.12
	IMG14	?	108.66	104.71	1.04	0089.36	–	–	00.43	004	00	00	002	002	1.00	0.00	0.00
		?	165.76	105.84	1.57	0137.80	–	–	00.61	007	01	00	004	005	1.25	0.50	0.60
		5400	168.70	105.36	1.60	0139.59	00.670	25	00.73	015	01	00	008	009	1.13	0.25	0.33
	IMG15	5400	215.95	096.21	2.24	0163.18	00.980	22	01.70	094	22	02	058	084	1.45	0.83	0.88
Poppe *et al.* (2019)	SPCTIN06	0420	–	–	–	–	–	–	00.15	010	03	00	007	010	1.46	0.92	0.95
		0840	–	–	–	–	–	–	00.43	022	15	00	019	034	1.81	1.62	1.34
		1260	–	–	–	–	–	–	00.56	020	22	00	021	043	2.05	2.10	1.53
		1680	–	–	–	–	–	–	00.76	021	23	03	022	051	2.32	2.36	1.59
		2100	–	–	–	–	–	–	01.00	026	38	03	032	076	2.38	2.56	1.66

(*Continued*)

Table 2. *Continued*.

References	Model	Time (s)	Forced fold geometry						Total fracture length (km)	Fracture connectivity							
			Length (cm)	Width (cm)	Length: width	Area (cm^2)	Maximum amplitude (cm)	Length: amplitude		I	Y	X	N_L	N_B	N_L/ N_B	C_L	C_B
Warsitzka *et al.* (2022)	Experiment 1B	4400	–	–	–	–	–	–	00.01	004	00	00	002	002	1.00	0.00	0.00
		4500	–	–	–	–	–	–	00.04	006	00	00	003	003	1.00	0.00	0.00
		4600	–	–	–	–	–	–	00.05	006	00	00	003	003	1.00	0.00	0.00
		4700	–	–	–	–	–	–	00.07	004	00	00	002	002	1.00	0.00	0.00
		4800	–	–	–	–	–	–	00.10	006	00	00	003	003	1.00	0.00	0.00
		4900	–	–	–	–	–	–	00.12	008	00	00	004	004	1.00	0.00	0.00
		5000	–	–	–	–	–	–	00.12	006	01	00	004	005	1.29	0.57	0.67
		5100	–	–	–	–	–	–	00.13	008	01	00	005	006	1.22	0.44	0.55
		5200	–	–	–	–	–	–	00.13	010	01	00	006	007	1.18	0.36	0.46
		5300	–	–	–	–	–	–	00.18	019	03	00	011	014	1.27	0.55	0.64
		5400	–	–	–	–	–	–	00.18	021	03	00	012	015	1.25	0.50	0.60
		5500	–	–	–	–	–	–	00.22	022	04	00	013	017	1.31	0.62	0.71
		5600	–	–	–	–	–	–	00.23	028	04	00	016	020	1.25	0.50	0.60
		5700	–	–	–	–	–	–	00.28	026	04	00	015	019	1.27	0.53	0.63
		5800	–	–	–	–	–	–	00.28	026	04	00	015	019	1.27	0.53	0.63
		5900	–	–	–	–	–	–	00.29	024	04	00	014	018	1.29	0.57	0.67
		6000	–	–	–	–	–	–	00.32	026	04	00	015	019	1.27	0.53	0.63
		6100	–	–	–	–	–	–	00.35	025	05	00	015	020	1.33	0.67	0.75
		6200	–	–	–	–	–	–	00.36	023	05	00	014	019	1.36	0.71	0.79
		6300	–	–	–	–	–	–	00.42	024	06	00	015	021	1.40	0.80	0.86
		6400	–	–	–	–	–	–	00.44	025	07	00	016	023	1.44	0.88	0.91
		6500	–	–	–	–	–	–	00.45	019	07	00	013	020	1.54	1.08	1.05
		6600	–	–	–	–	–	–	00.47	019	09	00	014	023	1.64	1.29	1.17
		6700	–	–	–	–	–	–	00.50	015	09	00	012	021	1.75	1.50	1.29
		6800	–	–	–	–	–	–	00.61	016	12	00	014	026	1.86	1.71	1.38
		6834	–	–	–	–	–	–	00.83	021	17	00	019	036	1.89	1.79	1.42
	Experiment 2B	3800	–	–	–	–	–	–	00.01	002	00	00	001	001	1.00	0.00	0.00
		3900	–	–	–	–	–	–	00.11	006	00	00	003	003	1.00	0.00	0.00
		4000	–	–	–	–	–	–	00.14	004	00	00	002	002	1.00	0.00	0.00
		4100	–	–	–	–	–	–	00.20	005	01	00	003	004	1.33	0.67	0.75
		4200	–	–	–	–	–	–	00.21	003	01	00	002	003	1.50	1.00	1.00
		4300	–	–	–	–	–	–	00.32	004	02	00	003	005	1.67	1.33	1.20
		4400	–	–	–	–	–	–	00.33	004	02	00	003	005	1.67	1.33	1.20
		4500	–	–	–	–	–	–	00.48	010	04	00	007	011	1.57	1.14	1.09
		4600	–	–	–	–	–	–	01.13	026	12	01	019	033	1.74	1.37	1.21
		4662	–	–	–	–	–	–	01.51	032	23	01	028	053	1.91	1.75	1.39
		4700	–	–	–	–	–	–	01.27	034	12	01	023	037	1.61	1.13	1.08

*No information available. Henriquet *et al.* (2019) do not state duration, and Montanari *et al.* (2017, 2020) images are screenshots from videos with no experiment timestamps.
†Indicates measurements could not be acquired from available images.

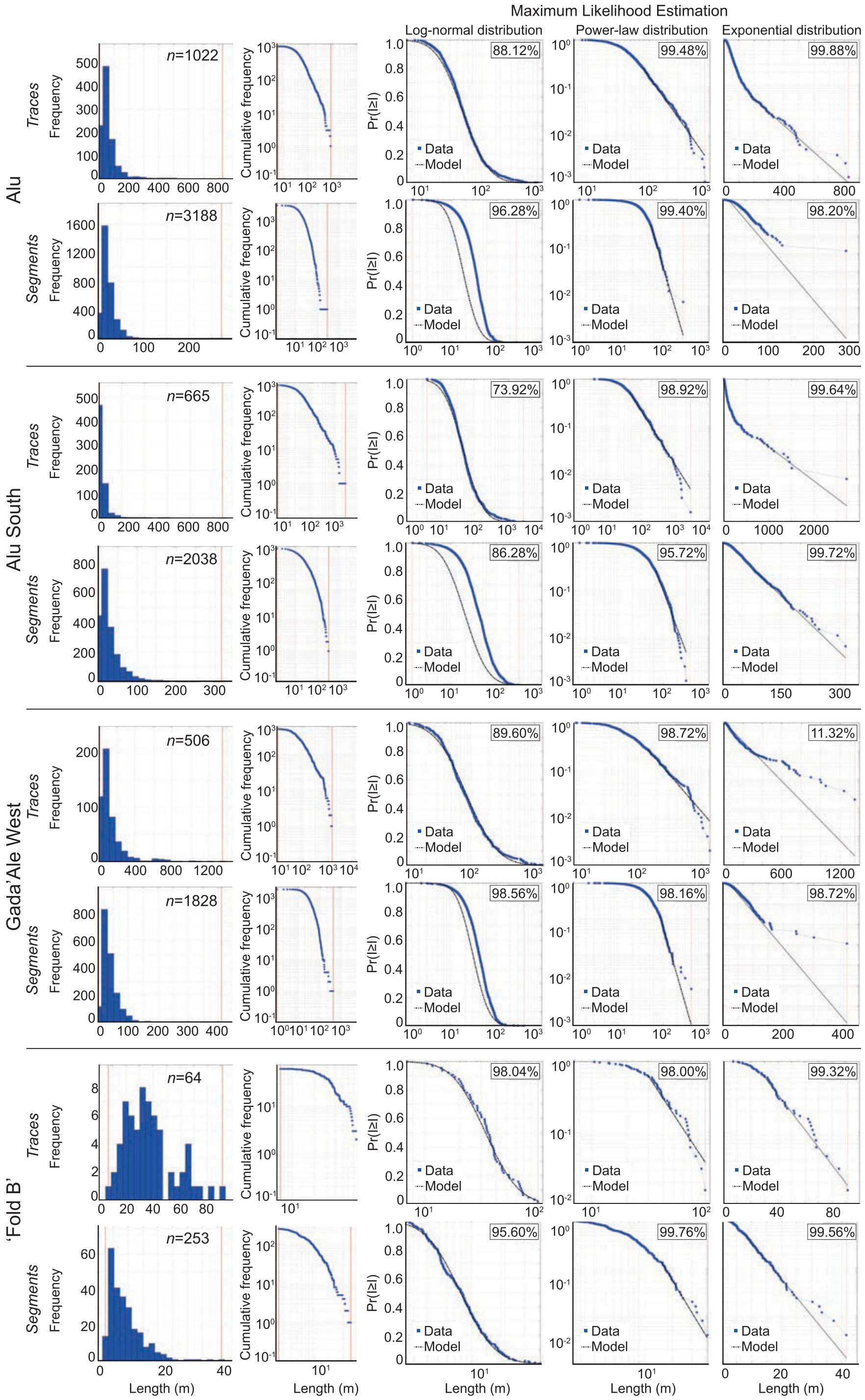

Fig. 9. Frequency histograms, cumulative frequency plots, and Maximum Likelihood Estimator probability (Pr) charts of fracture trace and segment length for Alu, Alu South, Gada'Ale West, and 'Fold B'. The probability charts test the fit of the data to a log-normal, power-lar, or exponential distribution (see Table 3). Here *n* is the number of fracture traces or segments mapped.

Table 3. Maximum Likelihood Estimation of fracture length distribution

Location	Probability fracture trace lengths conform to defined distribution			Probability fracture segment lengths conform to defined distribution		
	Log-normal (%)	Power-law (%)	Exponential (%)	Log-normal (%)	Power-law (%)	Exponential (%)
Alu	88.12	99.48	99.88	96.28	99.40	98.20
Alu South	73.92	98.92	99.64	86.28	95.72	99.72
Borale Ale	98.88	99.56	99.64	03.80	98.12	97.36
Gada East	98.68	99.88	50.44	91.68	97.04	96.36
Gada West	89.60	98.72	11.32	98.56	98.16	98.72
Dallol	99.00	99.84	99.76	98.60	97.36	74.40
Cordon	99.28	99.32	77.40	73.84	98.68	97.72
West Mata	98.88	99.64	94.72	98.92	98.20	98.96
‘Fold B’	98.04	98.00	99.32	95.60	99.76	99.56

support previous work that shows it is often the behaviour of the deforming rock volume during bending, itself a function of lithology, size of the forcing feature, and strain rate, which primarily controls forced folding and fracturing (e.g. Pollard and Johnson 1973; Stearns 1978; Gholipour *et al.* 2016; Wilson *et al.* 2016).

Fracture length distribution

The fracture length distribution of a sample set is often used to predict fracture network characteristics at smaller and/or larger scales (e.g. Bonnet *et al.* 2001). By using a robust statistical approach to assess probability of fit to different distributions (Rizzo *et al.* 2017), I show that most intrusion-induced forced folds studied contain fracture networks with trace and segment lengths compatible with a power-law relationship (Fig. 9; Table 3; Supplementary Figs S3 and S4). Yet it should be noted that for some datasets, log-normal (e.g. Dallol segment lengths) or exponential (e.g. Alu trace lengths) distributions appear more probable fits (Fig. 9; Table 3). A limitation with this analysis is that the resolution of the data may mean short fracture traces or segments are under-sampled (Fig. 9; Supplementary Figs S3 and S4), which can cause power-law distributions to appear log-normal (Bonnet *et al.* 2001).

Fracture connectivity

My data reveal that the connectivity of fracture networks across the tops of dome-like natural and

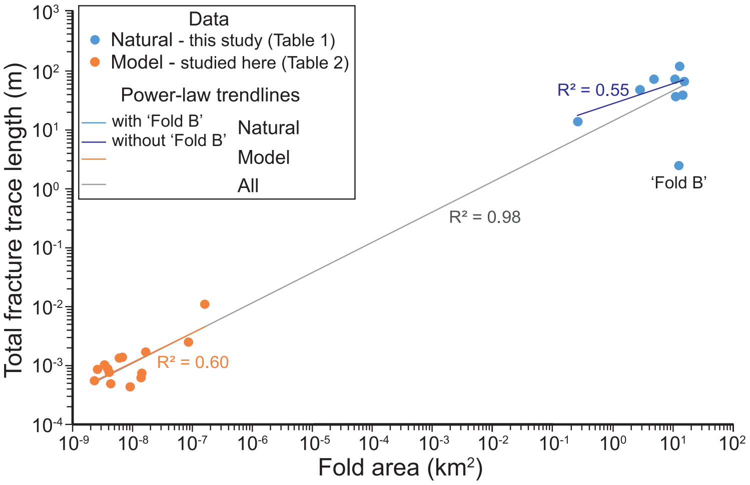

Fig. 10. Plot of forced fold area and total fracture trace length (see Tables 1 & 2 for data). ‘Fold B’ is not included in the calculation of the power-law trend for the natural forced fold data as its seismic resolution limits recognition of small-scale fractures.

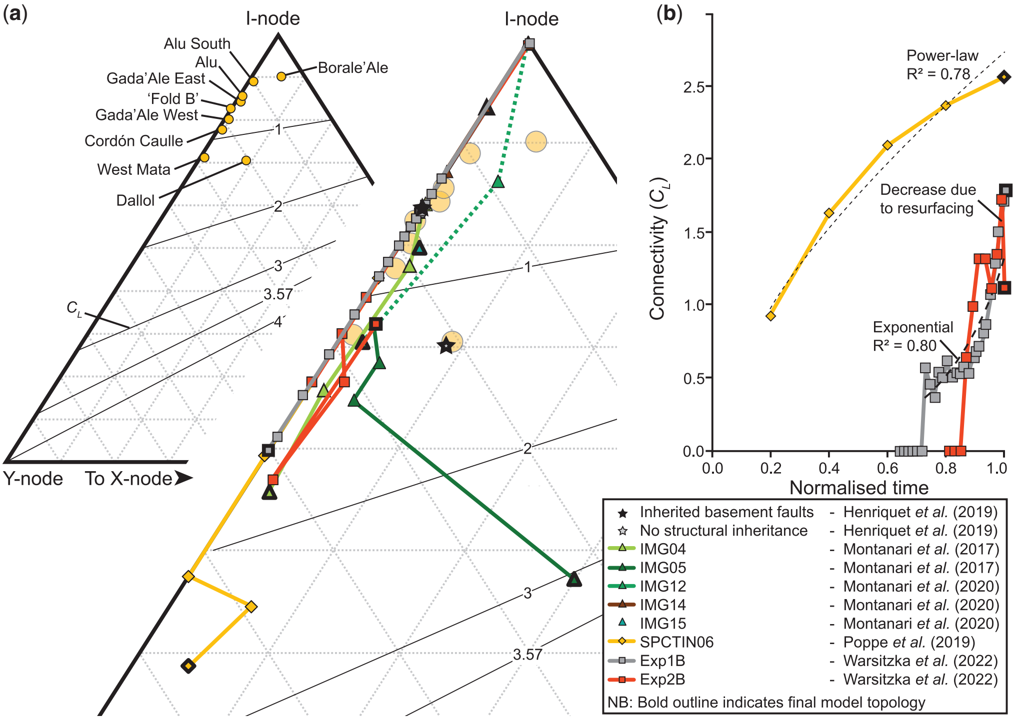

Fig. 11. (**a**) Ternary diagrams showing the proportion of I-, Y-, and X-nodes for each forced fold compared to contours showing the number of connections per line (C_L). Where images of modelled forced folds were acquired at different timestamps, the evolution of connectivity can be constrained. (**b**) Plot of connectivity against the normalized time for Exp1B and Exp2B (Warsitzka *et al.* 2022) and SPCTIN06 (Poppe *et al.* 2019), showing its evolution can be described by power-law or exponential relationships. Reductions in connectivity may be attributed to resurfacing of the forced fold by erupted products (see Fig. 3a.)

modelled forced folds tends to remain relatively low (C_L <3.01 and C_B <1.66; Fig. 11; Tables 1 & 2) (see Sanderson and Nixon 2015 and references therein). These results contrast with field-based analyses of a forced monocline above the outer edge of Trachyte Mesa intrusion, Utah, which show fractures and deformation bands are locally well-connected (Wilson *et al.* 2021). There are several possible reasons for these disparities in fracture connectivity. Firstly, the remote sensing and seismic reflection data I use to analyse natural forced folds have limited resolutions of metres to tens of metres (e.g. Fig. 4a) (e.g. Hansen and Cartwright 2006). It is thus plausible that unidentified fractures may be present, or identified fractures extend further, at scales below these data resolutions, which could lead to an increase in connectivity (e.g. Nixon *et al.* 2012). Secondly, my study distils a connectivity value for the entire top surface of each forced fold, obscuring zones where connectivity may locally be enhanced due to relatively higher fracture intensity, density, and/or fold curvature (e.g. Lisle 1999; Wilson *et al.* 2021); future work should focus on partitioning intrusion-induced forced folds, likely based on variations in curvature (e.g. comparing flat-topped and dome-like folds), to further assess connectivity patterns. Finally, I analyse fracture patterns on the top surface of forced folds, whereas the analyses of Trachyte Mesa examined fractures and deformation bands expressed on rock walls that form a cross-section through the monoclinal rim of a flat-topped forced fold (Wilson *et al.* 2021); that is, my work provides some insight into the lateral connectivity of intrusion-induced, dome-like forced fold fracture networks, but Wilson *et al.* (2021) provide a robust assessment of vertical connectivity in flat-topped folds. Overall, comparing our work demonstrates that ground-truthing is required to test remotely determined connectivity of fracture networks (Wilson *et al.* 2021). Furthermore, it will be crucial to establish how connectivity varies in 3D across entire forced folds (Wilson *et al.* 2021), which will require integrating analyses of well-exposed forced folds and those imaged in 3D seismic reflection data.

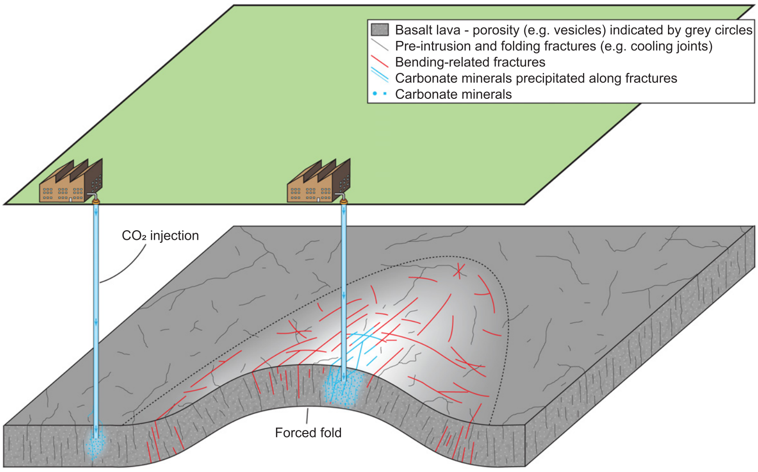

Fig. 12. Schematic showing bending-related fractures within basalt lava across a forced fold can enhance permeability and storage potential by providing fluid pathways and precipitation sites for CO_2 in addition to typically expected fracture sets (e.g. cooling joints) and porosity (inspired by Cosgrove and Ameen 1999; Gislason and Oelkers 2014).

An opportunity for CO_2 storage?

Successful sequestration of CO_2 through *in situ* mineral carbonation in basaltic rocks has opened up lava fields and volcanoes as potential exploration targets for CO_2 storage (e.g. Matter *et al.* 2016; Holford *et al.* 2021; Raza *et al.* 2022; Fedorik *et al.* 2023). This method typically relies on injection of either water and dissolved CO_2, or supercritical CO_2, into basalts that the fluids react with to permanently fix CO_2 in carbonate minerals (Fig. 12) (e.g. McGrail *et al.* 2014; Snæbjörnsdóttir *et al.* 2020). Permeability of the basalts is thus key as it enables fluid to flow away from injection sites, and increases the surface area of the rock that fluids can react with (e.g. Fedorik *et al.* 2023). Basalt lavas often contain a variety of fracture sets (e.g. cooling joints) and porosity (Fig. 12) (e.g. Snæbjörnsdóttir *et al.* 2018; Holford *et al.* 2021), but those within intrusion-induced forced folds (e.g. in the EAVS) will contain additional fracture sets due to bending-related stresses (e.g. Figs 5, 6 & 12). Given forced folds can also form suitable fluid traps, if reservoirs and seals are in place, it seems reasonable that those containing basaltic lava flows may form promising CO_2 storage targets (Fig. 12).

Conclusions

Intrusion-induced forced folds commonly contain an array of fractures generated by bending-related stresses during uplift. Coupled with the flat-topped or dome-like geometry of these forced folds, the presence of complex fracture networks suggests that they may form suitable pathways and traps for fluid flow. By comparing natural forced folds developed recently with those produced in physical experiments, I show that: (1) there is a positive relationship between forced fold length and amplitude, similar to that of laccolith and sill length to thickness relationships; (2) fracture networks comprise traces and segments with variable orientations and lengths, the latter of which predominantly conforming to power-law distributions; (3) fracture intensity and density generally increases with fold curvature and/or the presence of major normal faults; and (4) connectivity across the top of forced folds appears relatively low, but this may be due to limitations in the resolution of the data used. Fold and fracture development appear to be largely independent of the mechanism driving uplift, instead being related to the behaviour of the deforming rock during bending; we can thus use forced folds at the surface to inform predictions regarding fracturing of subsurface forced folds if they share similar host rock geology. Critically, intrusion-induced forced folds should be considered as exploration targets in the search for water aquifers, geothermal potential, and minerals/metals. Fracturing induced by bending may also increase the permeability of lavas within forced folds, potentially enhancing their suitability for CO_2 storage.

Acknowledgements Simon Holford is thanked for editorial handling, and Penelope Wilson and two anonymous reviewers are thanked for their constructive comments.

Competing interests

The authors declare that they have no known competing financial interests or personal relationships that could have appeared to influence the work reported in this paper.

Author contributions

CM: conceptualization (lead), data curation (lead), formal analysis (lead), investigation (lead), methodology (lead), project administration (lead), writing – original draft (lead), writing – review & editing (lead).

Funding

The Natural Environment Research Council has supported Craig Magee with funding for this paper.

Data availability

All satellite and bathymetry data used are available through either ArcGIS Pro, Google Earth, EarthExplorer (https://earthexplorer.usgs.gov/), or the Marine Geoscience Data System (https://www.marine-geo.org/tools/search/DataSets.php?data_set_uids=24446,24447). Seismic reflection and physical model data are published, with some of the images used taken from associated supplementary files. The vertices of fractures mapped in this work are provided as text or.svg files, ready for import into FracPaQ, in the Supplementary Material. Any other data is provided in the Figures and Tables.

References

Albino, F. and Biggs, J. 2021. Magmatic processes in the East African Rift system: insights from a 2015–2020 Sentinel-1 InSAR survey. *Geochemistry, Geophysics, Geosystems*, **22**, e2020GC009488, https://doi.org/10.1029/2020GC009488

Amelung, F., Oppenheimer, C., Segall, P. and Zebker, H. 2000. Ground deformation near Gada 'Ale Volcano, Afar, observed by radar interferometry. *Geophysical Research Letters*, **27**, 3093–3096, https://doi.org/10.1029/2000GL008497

Barberi, F. and Varet, J. 1970. The Erta Ale volcanic range (Danakil depression, northern afar, Ethiopia). *Bulletin Volcanologique*, **34**, 848–917, https://doi.org/10.1007/BF02596805

Bastow, I.D., Booth, A.D. *et al*. 2018. The development of late-stage continental breakup: seismic reflection and borehole evidence from the Danakil Depression, Ethiopia. *Tectonics*, **37**, 2848–2862, https://doi.org/10.1029/2017TC004798

Bonnet, E., Bour, O., Odling, N.E., Davy, P., Main, I., Cowie, P. and Berkowitz, B . 2001. Scaling of fracture systems in geological media. *Reviews of Geophysics*, **39**, 347–383, https://doi.org/10.1029/1999RG000074

Brown, A.R. 2011. *Interpretation of Three-Dimensional Seismic Data*, 6th edn. AAPG and SEG, Oklahoma, USA.

Bunger, A.P. and Cruden, A.R. 2011. Modeling the growth of laccoliths and large mafic sills: role of magma body forces. *Journal of Geophysical Research: Solid Earth*, **116**, B02203, https://doi.org/10.1029/2010JB007648

Castro, J.M., Cordonnier, B., Schipper, C.I., Tuffen, H., Baumann, T.S. and Feisel, Y. 2016. Rapid laccolith intrusion driven by explosive volcanic eruption. *Nature Communications*, **7**, 13585, https://doi.org/10.1038/ncomms13585

Chadwick, W.W., Jr, Rubin, K.H., Merle, S.G., Bobbitt, A.M., Kwasnitschka, T. and Embley, R.W. 2019. Recent eruptions between 2012 and 2018 discovered at west Mata submarine volcano (NE Lau Basin, SW Pacific) and characterized by new ship, AUV, and ROV data. *Frontiers in Marine Science*, **495**, https://doi.org/10.3389/fmars.2019.00495

Cosgrove, J. 2015. The association of folds and fractures and the link between folding, fracturing and fluid flow during the evolution of a fold–thrust belt: a brief review. *Geological Society, London, Special Publications*, **421**, 41–68, https://doi.org/10.1144/SP421.11

Cosgrove, J.W. and Ameen, M.S. 1999. A comparison of the geometry, spatial organization and fracture patterns associated with forced folds and buckle folds. *Geological Society, London, Special Publications*, **169**, 7–21, https://doi.org/10.1144/gsl.sp.2000.169.01.02

Cosgrove, J.W. and Hillier, R.D. 1999. Forced-fold development within Tertiary sediments of the Alba Field, UKCS: evidence of differential compaction and post-depositional sandstone remobilization. *Geological Society, London, Special Publications*, **169**, 61–71, https://doi.org/10.1144/gsl.sp.2000.169.01.05

Cruden, A.R., McCaffrey, K.J. and Bunger, A.P. 2018. Geometric scaling of tabular igneous intrusions: implications for emplacement and growth. *In*: Breitkreuz, C. and Rocchi, S. (eds) *Physical Geology of Shallow Magmatic Systems: Dykes, Sills and Laccoliths*. Springer, 11–38.

Dimmen, V., Rotevatn, A. and Nixon, C.W. 2020. The relationship between fluid flow, structures, and depositional architecture in sedimentary rocks: an example-based overview. *Geofluids*, **2020**, 1–19, https://doi.org/10.1155/2020/3506743

Dobb, E.M., Magee, C., Jackson, C.A.-L., Lathrop, B. and Köpping, J. 2022. Impact of igneous intrusion and associated ground deformation on the stratigraphic record. *Geological Society, London, Special Publications*, **525**, https://doi.org/10.1144/SP525-2021-115

Fedorik, J., Delaunay, A.J.R. *et al*. 2023. Structure and fracture characterization of the Jizan group: implications for subsurface CO_2 basalt mineralization. *Frontiers in Earth Science*, **10**, https://doi.org/10.3389/feart.2022.946532

Fossen, H. and Bale, A. 2007. Deformation bands and their influence on fluid flow. *AAPG Bulletin*, **91**, 1685–1700, https://doi.org/10.1306/07300706146

Gholipour, A.M., Cosgrove, J.W. and Ala, M. 2016. New theoretical model for predicting and modelling fractures in folded fractured reservoirs. *Petroleum Geoscience*, **22**, 257–280, https://doi.org/10.1144/petgeo2013-055

Goulty, N.R. and Schofield, N. 2008. Implications of simple flexure theory for the formation of saucer-shaped sills. *Journal of Structural Geology*, **30**, 812–817, https://doi.org/10.1016/j.jsg.2008.04.002

Gislason, S.R. and Oelkers, E.H. 2014. Carbon storage in basalt. *Science (New York, NY)*, **344**, 373–374, https://doi.org/10.1126/science.1250828

Hansen, D.M. and Cartwright, J. 2006. The three-dimensional geometry and growth of forced folds above saucer-shaped igneous sills. *Journal of*

Structural Geology, **28**, 1520–1535, https://doi.org/10.1016/j.jsg.2006.04.004

Healy, D., Rizzo, R.E. *et al*. 2017. FracPaQ: a MATLAB™ toolbox for the quantification of fracture patterns. *Journal of Structural Geology*, **95**, 1–16, https://doi.org/10.1016/j.jsg.2016.12.003

Henriquet, M., Dominguez, S., Barreca, G., Malavieille, J., Cadio, C. and Monaco, C. 2019. Deep origin of the dome-shaped Hyblean Plateau, southeastern Sicily: a new tectono-magmatic model. *Tectonics*, **38**, 4488–4515, https://doi.org/10.1029/2019TC005548

Holford, S.P., Schofield, N., MacDonald, J.D., Duddy, I.R. and Green, P.F. 2012. Seismic analysis of igneous systems in sedimentary basins and their impacts on hydrocarbon prospectivity: examples from the southern Australian margin. *APPEA Journal*, **52**, 23, https://doi.org/10.1071/AJ11017

Holford, S., Schofield, N., Bunch, M., Bischoff, A. and Swierczek, E. 2021. Storing CO_2 in buried volcanoes. *The APPEA Journal*, **61**, 626–631, https://doi.org/10.1071/AJ20056

Jackson, C.A.-L., Schofield, N. and Golenkov, B. 2013. Geometry and controls on the development of igneous sill–related forced folds: a 2-D seismic reflection case study from offshore southern Australia. *Geological Society of America Bulletin*, **125**, 1874–1890, https://doi.org/10.1130/b30833.1

Jackson, M.D. and Pollard, D.D. 1990. Flexure and faulting of sedimentary host rocks during growth of igneous domes, Henry Mountains, Utah. *Journal of Structural Geology*, **12**, 185–206, https://doi.org/10.1016/0191-8141(90)90004-I

Jackson, C.A.-L., Magee, C. and Jacquemyn, C. 2020. Rift-related magmatism influences petroleum system development in the NE Irish Rockall Basin, offshore Ireland. *Petroleum Geoscience*, **26**, 511–524, https://doi.org/10.1144/petgeo2018-020

Kumar, P.C., Niyazi, Y., Eruteya, O.E., Moscariello, A., Warne, M., Ierodiaconou, D. and Sain, K. 2022. Anatomy of intrusion related forced fold in the offshore Otway Basin, SE Australia. *Marine and Petroleum Geology*, **141**, 105719, https://doi.org/10.1016/j.marpetgeo.2022.105719

Lisle, R.J. 1999. Predicting patterns of strain from three-dimensional fold geometries: neutral surface folds and forced folds. *Geological Society, London, Special Publications*, **169**, 213–221, https://doi.org/10.1144/gsl.sp.2000.169.01.16

López-García, J.M., Moreira, D., Benzerara, K., Grunewald, O. and López-García, P. 2020. Origin and evolution of the halo-volcanic complex of Dallol: proto-volcanism in Northern Afar (Ethiopia). *Frontiers in Earth Science*, **351**, https://doi.org/10.3389/feart.2019.00351

Magee, C., Briggs, F. and Jackson, C.A.-L. 2013. Lithological controls on igneous intrusion-induced ground deformation. *Journal of the Geological Society, London*, **170**, 853–856, https://doi.org/10.1144/jgs2013-029

Magee, C., Muirhead, J.D. *et al*. 2016. Lateral magma flow in mafic sill complexes. *Geosphere*, **12**, 809–841, https://doi.org/10.1130/GES01256.1

Magee, C., Bastow, I.D., de Vries, B.V.W., Jackson, C.A.-L., Hetherington, R., Hagos, M. and Hoggett, M. 2017. Structure and dynamics of surface uplift induced by incremental sill emplacement. *Geology*, **45**, 431–434, https://doi.org/10.1130/G38839.1

Magee, C., Hoggett, M., Jackson, C.A.-L. and Jones, S.M. 2019. Burial-related compaction modifies intrusion-induced forced folds: implications for reconciling roof uplift mechanisms using seismic reflection data. *Frontiers in Earth Science*, **7**, https://doi.org/10.3389/feart.2019.00037

Matter, J.M., Stute, M. *et al*. 2016. Rapid carbon mineralization for permanent disposal of anthropogenic carbon dioxide emissions. *Science (New York, NY)*, **352**, 1312–1314, https://doi.org/10.1126/science.aad8132

McCaffrey, K.J.W. and Petford, N. 1997. Are granitic intrusions scale invariant?. *Journal of the Geological Society, London*, **154**, 1–4, https://doi.org/10.1144/gsjgs.154.1.0001

McGrail, B.P., Spane, F.A., Amonette, J.E., Thompson, C. and Brown, C.F. 2014. Injection and monitoring at the Wallula basalt pilot project. *Energy Procedia*, **63**, 2939–2948, https://doi.org/10.1016/j.egypro.2014.11.316

Meng, Q. and Hodgetts, D. 2020. Forced folding and fracturing induced by differential compaction during post-depositional inflation of sandbodies: insights from numerical modelling. *Marine and Petroleum Geology*, **112**, 104052, https://doi.org/10.1016/j.marpetgeo.2019.104052

Montanari, D., Bonini, M., Corti, G., Agostini, A., Del Ventisette, C.J.J.O.V. and Research, G. 2017. Forced folding above shallow magma intrusions: insights on supercritical fluid flow from analogue modelling. *Journal of Volcanology and Geothermal Research*, **345**, 67–80, https://doi.org/10.1016/j.jvolgeores.2017.07.022

Montanari, D., Del Ventisette, C. and Bonini, M. 2020. Lateral magma migration through interconnected sills: evidence from analogue modeling. *Earth and Planetary Science Letters*, **551**, 116568, https://doi.org/10.1016/j.epsl.2020.116568

Morgan, S., Stanik, A., Horsman, E., Tikoff, B., de Saint Blanquat, M. and Habert, G. 2008. Emplacement of multiple magma sheets and wall rock deformation: Trachyte Mesa intrusion, Henry Mountains, Utah. *Journal of Structural Geology*, **30**, 491–512, https://doi.org/10.1016/j.jsg.2008.01.005

Mynatt, I., Bergbauer, S. and Pollard, D.D. 2007. Using differential geometry to describe 3-D folds. *Journal of Structural Geology*, **29**, 1256–1266, https://doi.org/10.1016/j.jsg.2007.02.006

Nixon, C.W., Sanderson, D.J. and Bull, J.M. 2012. Analysis of a strike-slip fault network using high resolution multibeam bathymetry, offshore NW Devon UK. *Tectonophysics*, **541**, 69–80, https://doi.org/10.1016/j.tecto.2012.03.021

Nobile, A., Pagli, C., Keir, D., Wright, T.J., Ayele, A., Ruch, J. and Acocella, V. 2012. Dike-fault interaction during the 2004 Dallol intrusion at the northern edge of the Erta Ale Ridge (Afar, Ethiopia). *Geophysical Research Letters*, **39**, https://doi.org/10.1029/2012GL053152

Pagli, C., Wright, T.J., Ebinger, C.J., Yun, S.-H., Cann, J.R., Barnie, T. and Ayele, A. 2012. Shallow axial magma chamber at the slow-spreading Erta Ale

Ridge. *Nature Geoscience*, **5**, 284–288, https://doi.org/10.1038/ngeo1414

Pearce, M.A., Jones, R.R., Smith, S.A. and McCaffrey, K.J. 2011. Quantification of fold curvature and fracturing using terrestrial laser scanning. *AAPG Bulletin*, **95**, 771–794, https://doi.org/10.1306/11051010026

Pollard, D.D. and Johnson, A.M. 1973. Mechanics of growth of some laccolithic intrusions in the Henry Mountains, Utah, II: bending and failure of overburden layers and sill formation. *Tectonophysics*, **18**, 311–354, https://doi.org/10.1016/0040-1951(73)90051-6

Poppe, S., Holohan, E.P. *et al.* 2019. An inside perspective on magma intrusion: quantifying 3D displacement and strain in laboratory experiments by dynamic x-ray computed tomography. *Frontiers in Earth Science*, **7**, 62, https://doi.org/10.3389/feart.2019.00062

Ramsey, J.G. 1968. *Folding and Fracturing of Rock*. The Blackburn Press, New Jersey.

Raza, A., Glatz, G., Gholami, R., Mahmoud, M. and Alafnan, S. 2022. Carbon mineralization and geological storage of CO_2 in basalt: mechanisms and technical challenges. *Earth-Science Reviews*, **229**, 104036, https://doi.org/10.1016/j.earscirev.2022.104036

Riley, M.S. 2005. Fracture trace length and number distributions from fracture mapping. *Journal of Geophysical Research: Solid Earth*, **110**, https://doi.org/10.1029/2004JB003164

Rizzo, R.E., Healy, D. and De Siena, L. 2017. Benefits of maximum likelihood estimators for fracture attribute analysis: implications for permeability and up-scaling. *Journal of Structural Geology*, **95**, 17–31, https://doi.org/10.1016/j.jsg.2016.12.005

Rodriguez Monreal, F., Villar, H., Baudino, R., Delpino, D. and Zencich, S. 2009. Modeling an atypical petroleum system: a case study of hydrocarbon generation, migration and accumulation related to igneous intrusions in the Neuquen Basin, Argentina. *Marine and Petroleum Geology*, **26**, 590–605, https://doi.org/10.1016/j.marpetgeo.2009.01.005

Sanderson, D.J. and Nixon, C.W. 2015. The use of topology in fracture network characterization. *Journal of Structural Geology*, **72**, 55–66, https://doi.org/10.1016/j.jsg.2015.01.005

Schutter, S.R. 2003. Hydrocarbon occurrence and exploration in and around igneous rocks. *Geological Society, London, Special Publications*, **214**, 7–33, https://doi.org/10.1144/gsl.sp.2003.214.01.02

Scott, S., Driesner, T. and Weis, P. 2015. Geologic controls on supercritical geothermal resources above magmatic intrusions. *Nature Communications*, **6**, 7837, https://doi.org/10.1038/ncomms8837

Segall, P. 2013. Volcano deformation and eruption forecasting. *Geological Society, London, Special Publications*, **380**, https://doi.org/10.1144/SP380.4

Snæbjörnsdóttir, S.Ó., Tómasdóttir, S. *et al.* 2018. The geology and hydrology of the CarbFix2 site, SW-Iceland. *Energy Procedia*, **146**, 146–157, https://doi.org/10.1016/j.egypro.2018.07.019

Snæbjörnsdóttir, S.Ó., Sigfússon, B., Marieni, C., Goldberg, D., Gislason, S.R. and Oelkers, E.H. 2020. Carbon dioxide storage through mineral carbonation. *Nature Reviews Earth and Environment*, **1**, 90–102, https://doi.org/10.1038/s43017-019-0011-8

Stearns, D.W. 1978. Faulting and forced folding in the Rocky Mountains foreland. *Geological Society of America Memoirs*, **151**, 1–38, https://doi.org/10.1130/MEM151-p1

Sullivan, C. and Kaszynski, A. 2019. PyVista: 3D plotting and mesh analysis through a streamlined interface for the Visualization Toolkit (VTK). *Journal of Open Source Software*, **4**, 1450, https://doi.org/10.21105/joss.01450

Tian, W., Li, X. and Wang, L. 2021. Forced fold amplitude and sill thickness constrained by wireline and 3-D seismic data suggest an elastic magma-induced deformation in Tarim Basin, NW China. *Minerals*, **11**, 293, https://doi.org/10.3390/min11030293

Tueckmantel, C., Fisher, Q.J., Manzocchi, T., Skachkov, S. and Grattoni, C.A. 2012. Two-phase fluid flow properties of cataclastic fault rocks: implications for CO_2 storage in saline aquifers. *Geology*, **40**, 39–42, https://doi.org/10.1130/G32508.1

van Wyk de Vries, B., Márquez, A., Herrera, R., Bruña, J.G., Llanes, P. and Delcamp, A. 2014. Craters of elevation revisited: forced-folds, bulging and uplift of volcanoes. *Bulletin of Volcanology*, **76**, 1–20, https://doi.org/10.1007/s00445-014-0875-x

Wadsworth, F.B., Llewellin, E.W. *et al.* 2022. A reappraisal of explosive–effusive silicic eruption dynamics: syn-eruptive assembly of lava from the products of cryptic fragmentation. *Journal of Volcanology and Geothermal Research*, **432**, 107672, https://doi.org/10.1016/j.jvolgeores.2022.107672

Warsitzka, M., Kukowski, N. and May, F. 2022. Patterns and failure modes of fractures resulting from forced folding of Cohesive Caprocks–Comparison of 2D v. 3D and Single-v. multi-layered analog experiments. *Frontiers in Earth Science*, **10**, 881134, https://doi.org/10.3389/feart.2022.881134

Watts, E.J., Gernon, T.M. *et al.* 2020. Evolution of the Alu-Dalafilla and Borale volcanoes, Afar, Ethiopia. *Journal of Volcanology and Geothermal Research*, **408**, 107094, https://doi.org/10.1016/j.jvolgeores.2020.107094

Weis, P. 2012. The dynamic interplay between saline fluid flow and rock permeability in magmatic–hydrothermal systems. *In*: Gleeson, T. and Ingebritse, S.E. *Crustal Permeability*. Wiley, 373–392, https://doi.org/10.1002/9781119166573.ch29

Wilson, P.I., McCaffrey, K.J. *et al.* 2016. Deformation structures associated with the Trachyte Mesa intrusion, Henry Mountains, Utah: implications for sill and laccolith emplacement mechanisms. *Journal of Structural Geology*, **87**, 30–46, https://doi.org/10.1016/j.jsg.2016.04.001

Wilson, P.I., Wilson, R.W., Sanderson, D.J., Jarvis, I. and McCaffrey, K.J. 2021. Analysis of deformation bands associated with the Trachyte Mesa intrusion, Henry Mountains, Utah: implications for reservoir connectivity and fluid flow around sill intrusions. *Solid Earth*, **12**, 95–117, https://doi.org/10.5194/se-12-95-2021

Zheng, W., Pritchard, M., Delgado, F. and Reath, K. 2020. Laccolith evolution during and after the 2011–12 eruption of Cordon Caulle volcano, Chile, from satellite feature-tracking, elevation, and thermal observations. *AGU Fall Meeting Abstracts*. San Francisco, USA, V004-0025.